Research Paper

Size-Tunable Gd₂O₃@Albumin Nanoparticles Conjugating Chlorin e6 for Magnetic Resonance Imaging-Guided Photo-Induced Therapy

Lijuan Zhou[1,5]*, Tao Yang[2]*, Junxing Wang[1]*, Qiaoli Wang[2], Xiaoyan Lv[2], Hengte Ke[2], Zhengqing Guo[3], Junkang Shen[1,5], Yong Wang[3✉], Chungen Xing[4✉], and Huabing Chen[2,3✉]

1. Department of Radiology, Second Affiliated Hospital of Soochow University, Suzhou215004, Jiangsu, China;
2. Jiangsu Key Laboratory of Translational Research and Therapy for Neuro-Psycho-Diseases, and College of Pharmaceutical Sciences, Soochow University, Suzhou 215123, Jiangsu, China;
3. School for Radiological & Interdisciplinary Sciences (RAD-X), Collaborative Innovation Center of Radiation Medicine of Jiangsu Higher Education Institutions, and School of Radiation Medicine and Protection, Soochow University, Suzhou 215123, Jiangsu, China;
4. Department of General Surgery, Second Affiliated Hospital of Soochow University, Suzhou 215004, Jiangsu, China;
5. Institute of Radiotherapy & Oncology, Soochow University, Suzhou 215004, Jiangsu, China.

*Equal contribution to this study.

✉ Corresponding authors: Dr. Yong Wang; School for Radiological & Interdisciplinary Sciences (RAD-X), Collaborative Innovation Center of Radiation Medicine of Jiangsu Higher Education Institutions, and School of Radiation Medicine and Protection, Soochow University, Suzhou 215123, Jiangsu, China. E-mail: wangyongac@gmail.com; Prof. Chungen Xing; Department of General Surgery, Second Affiliated Hospital of Soochow University, Suzhou 215004, Jiangsu, China; E-mail: xingcg@126.com. Prof. Huabing Chen; Jiangsu Key Laboratory of Translational Research and Therapy for Neuro-Psycho-Diseases, and College of Pharmaceutical Sciences, Soochow University, Suzhou 215123, Jiangsu, China. E-mail: chenhb@suda.edu.cn.

Abstract

Protein nanoparticles as nanocarriers are of particular interest in the field of cancer therapy. Nevertheless, so far a facile fabrication of theranostic protein nanoparticles have been explored with limited success for cancer imaging and therapy. In this work, we demonstrate the controllable synthesis of size-tunable Gd₂O₃@albumin conjugating photosensitizer (PS) (GA-NPs) using hollow albumin as the nanoreactor for magnetic resonance imaging (MRI)-guided photo-induced therapy. The growth of Gd₂O₃ nanocrystals within the hollow nanoreactors is well regulated through reaction time, and a typical PS (e.g. chlorin e6) is further conjugated with the protein corona of the nanoreactor through facile chemical coupling, followed by the formation of theranostic GA-NPs. GA-NPs exhibit good longitudinal relaxivity, ideal photostability, enhanced cellular uptakes, and preferable size-dependent tumor accumulation. Moreover, GA-NPs effectively generate remarkable photothermal effect, intracellular reactive oxygen species from Ce6, and subsequent cytoplasmic drug translocation, thereby leading to severe synergistic photothermal and photodynamic cell damages. Consequently, GA-NPs exhibit an *in vivo* size-dependent MRI capacity with enhanced imaging contrast for effective tumor localization, and also generate a potent synergistic photodynamic therapy/photothermal therapy efficacy under irradiation owing to their enhanced tumor accumulation and strong photo-induced cytotoxicity. These results suggest that GA-NPs can act as a promising theranostic protein nanoplatform for cancer imaging and photo-induced therapy.

Key words: albumin nanoreactor, gadolinium oxide, photosensitizer, magnetic resonance imaging, photodynamic therapy.

Introduction

Photodynamic therapy (PDT) has extensively been explored as a non-invasive modality for selectively treating tumor, which utilizes photosen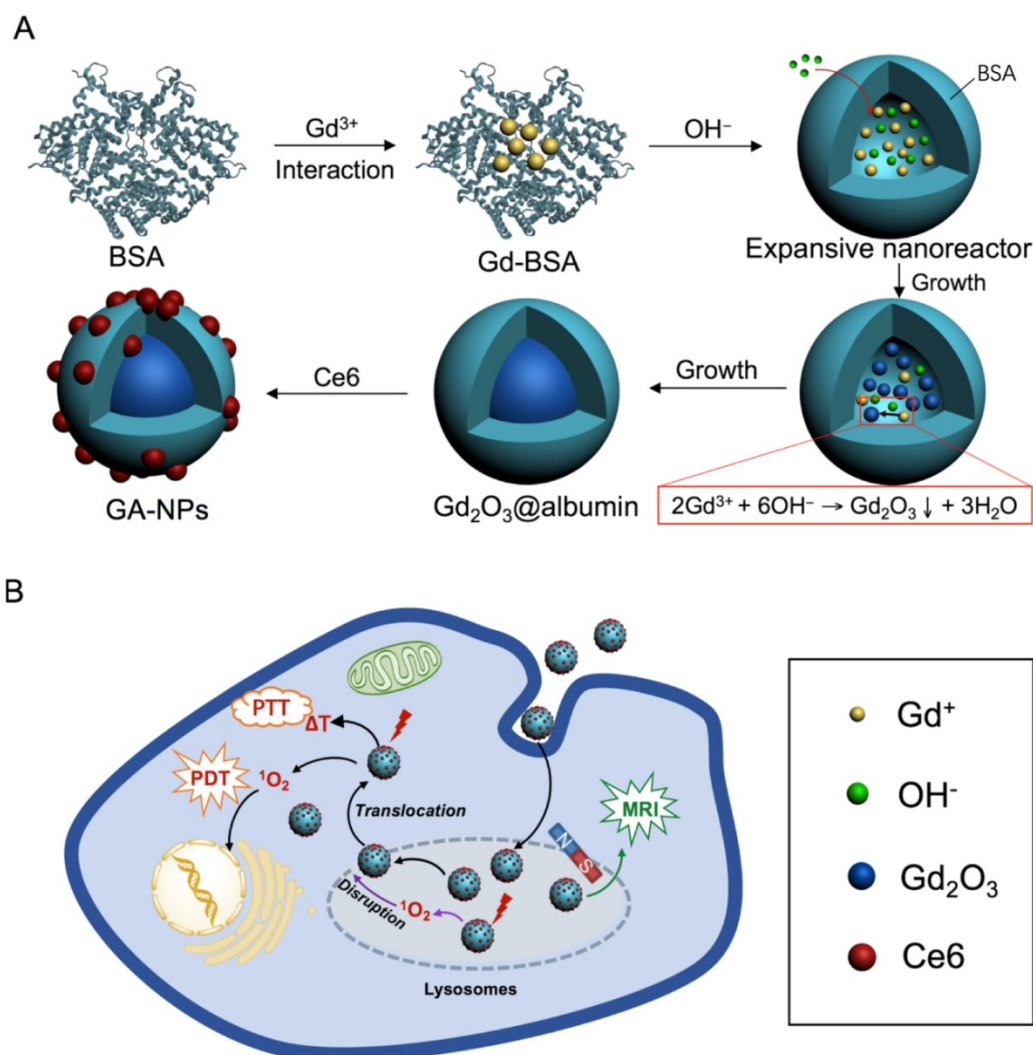sitizers (PS) such as porphyrin, chlorin e6 (Ce6) and phthalocyanines to generate reactive oxygen species (ROS) such as singlet oxygen for damaging tumor cells without injuring surrounding healthy tissues under light irradiation. [1-7] Essentially,

PS can transfer light energy to molecular oxygen, thereby generating singlet oxygen to effectively trigger cell apoptosis for cancer therapy.[8-10] To date, several factors have been found to act as the fundamental roles in PDT efficacy including photostability, tumor accumulation, intracellular drug translocation, as well as precise tumor localization and treatment, which are considered as effective strategies to improve the photophysicochemical and photobiological features of PS. Recently, the nanocarriers including micelles, vesicles, and inorganic nanomaterials have extensively been developed to improve the physicochemical features and *in vivo* pharmacokinetic performances for enhanced PDT efficacy, which can further be boosted through the effective tumor imaging with increased sensitivity or spatial resolution from the co-encapsulated imaging agents.[11-19] The imaging characteristics of the nanocarriers can provide good tumor localization for achieving imaging-guided PDT treatment and therapeutic monitoring.

Despite recent exciting progress in the development of theranostic nanocarriers for PDT, there are several limitation in the following aspects: firstly, PS frequently encounter the photo-bleaching under irradiation owing to the decrease of their absorbance, which might significantly impair their PDT efficacy;[8, 12] Secondly, singlet oxygen generally possess a very short half-life time of less than 40 ns and limited diffusion distance of 10 ~ 20 nm, which thus demand an effective intracellular translocation of PS to cytoplasm to maximize the accessibility of singlet oxygen to target organelles such as mitochondria and nucleus;[8, 9] Thirdly, the existing theranostic nanoparticles are generally fabricated through the co-encapsulation of PS and imaging agents within the vehicles, which might cause their inconsistency of pharmacokinetic behaviors upon release from the vehicles.[20-23] Consequently, it is highly necessary to develop a theranostic nanoplatform that can effectively achieve both enhanced imaging characteristics and effective intracellular delivery of PS for imaging-guided PDT treatment through a facile fabrication strategy.

Recently, many proteins such as human serum albumin and CD2 protein have extensively been fabricated as the nanoparticles to incorporate various payloads including anticancer compounds, fluorescent dyes, and metal ions through physical encapsulation, covalent coupling, or affinity binding for theranostic application.[24-29] In particular, some proteins can display a hollow expansive protein conformation through unfolding process in some special environments such as basic solution owing to their excess charged groups and chain flexibility, which can provide a nanoscale expanded cavity to accommodate single nanoparticle of the payload such as anticancer compound or inorganic imaging nanomaterial for therapeutic or imaging purpose.[24, 28, 30-32] For instance, bovine serum albumin (BSA) and ferritin can effectively act as a hollow nanoreactor to facilitate the growth of metal ions into the metal clusters (e.g. Au clusters) and metallic oxides with several nanometers through the affinity binding of metal ions with abundant active groups of proteins such as carboxylic group, and subsequent growth in their hollow nanocages for fluorescence or magnetic resonance imaging (MRI).[24, 28, 33, 34] Ferritin can also act as protein vehicle to incorporate anticancer compounds within their hollow cavity (~8 nm in diameter) for enhanced chemotherapy.[31, 32] More interestingly, these hollow proteins as the nanocarrier are generally able to possess unique mono-dispersive size distribution, controllable encapsulation, facile and reproducible fabrication, which is highly potential to facilitate their diagnostic or therapeutic capacities. Consequently, it is highly desired to provide the insight into the fabrication strategy of protein nanoparticles to integrate imaging agent and PS to achieve both enhanced imaging capacity and effective intracellular delivery of PS for imaging-guided photo-induced therapy. Herein, we synthesize size-tunable Gd_2O_3@albumin conjugating PS (GA-NPs) using albumin as a nanoreactor for MRI-guided photo-induced therapy (Scheme 1). We effectively regulate the growth of Gd_2O_3 nanocrystals within the nanoreactor through reaction time, which was further conjugated with a typical PS (e.g. Ce6) through facile chemical coupling, followed by the formation of theranostic GA-NPs. GA-NPs exhibit good longitudinal relaxivity, ideal photostability, and enhanced cellular uptakes, as well as preferable size-dependent tumor accumulation. Moreover, GA-NPs effectively generate intracellular ROS from PS that subsequently trigger the intracellular translocation from the lysosomes to cytoplasm, and simultaneously produce distinct photothermal effect under irradiation, thereby leading to severe photodynamic and photothermal cytotoxicity. Consequently, GA-NPs generate the preferable *in vivo* MRI capacity with enhanced imaging contrast for effective tumor localization, and simultaneously exhibit potent synergistic PDT and photothermal therapy (PTT) upon irradiation owing to their preferable tumor accumulation and strong photo-cytotoxicity.

Scheme 1. Schematic illustration of size-tunable Gd$_2$O$_3$@albumin conjugating PS synthesized through albumin nanoreactor for MRI-guided photo-induced cancer therapy.

Results and Discussion

Synthesis and Characterization

An albumin nanoreactor was employed to synthesize Gd$_2$O$_3$ nanocrystals within their expansive cavity (Scheme 1A). Briefly, BSA was mixed with Gd(NO$_3$)$_3$ under vigorous vortexing in aqueous solution. The albumin could trigger metal ion complex through abundant active groups such as sulfhydryl and carboxyl groups in albumin.[28, 30, 35] Subsequently, NaOH was used to cause the expansion of albumin at pH 12 through unfolding process (Figure S1), and simultaneously trigger the nucleation and growth of Gd$_2$O$_3$ through the precipitation reaction of $2Gd(NO_3)_3 + 6NaOH = Gd_2O_3 + 6NaNO_3 + 3H_2O$ within hollow expanded albumin,[36] followed by the formation of Gd$_2$O$_3$ nanocrystals within albumin (Gd$_2$O$_3$@albumin). In this reaction, reaction time was found to be able to regulate the formation of Gd$_2$O$_3$ nanocrystals (Figure 1). The Gd$_2$O$_3$

nanocrystals with the average diameters of 3.0 ± 0.5 nm, 4.7 ± 0.5 nm, and 5.4 ± 0.4 nm were obtained after 1 h, 4 h, and 8 h reaction, respectively (Figure 1A-C), while the reaction of 12 h led to the formation of Gd$_2$O$_3$ nanocrystals with 10.1 ± 1.2 nm (Figure 1D). Possibly, most of Gd^{3+} ions were distributed in the expanded cavity of nanoreactor and thus need excessive hydroxyl ions to cause continuous growth of Gd$_2$O$_3$ nanocrystals through the precipitation reaction.[37] Hence, reaction time allows continuous growth of Gd$_2$O$_3$ nanocrystals with various diameters through effective precipitation reaction in the hollow nanoreactor.[24, 36] Scanning electron microscopy (SEM) imaging shows that Gd$_2$O$_3$@BSA possess the average diameter of 23.3 ± 1.2 nm (Figure 1E), implying that Gd$_2$O$_3$@BSA have a core-shell nanostructure, and the single hollow albumin nanocage as a shell is able to accommodate one Gd$_2$O$_3$ nanocrystal within it. DLS measurement shows that Gd$_2$O$_3$@albumin obtained from 12 h reaction exhibited the hydrodynamic size of

25.0 nm with zeta potential of -27.5 mV (Figure 1F and and Figure S2). The suitable hydrodynamic diameter might have a potential capacity to generate enhanced permeation and retention (EPR) effect for cancer targeting.[36] Circular dichroism spectra show that Gd$_2$O$_3$@BSA exhibited a negligible change in the secondary structure of BSA, suggesting that the synthetic process has no significant influence on the nature of BSA (Figure S3).

High-resolution transmission electron microscopy (HR-TEM) imaging shows that Gd$_2$O$_3$@albumin with 10.1 ± 1.2 nm diameter had a well-defined lattice structure with the lattice fringe of d_{111}=3.12 ± 0.15 Å (Figure 2A), which was in agreement with that of reported Gd$_2$O$_3$ phase.[36] To explore the possibility of Gd$_2$O$_3$@albumin with various particle size as MR imaging agent, their longitudinal proton relaxation time (T_1) was measured using T_1-weighted mapping at the magnetic

field of 1.5 T. Gd$_2$O$_3$@albumin with 4.7 nm, 5.4 nm, and 10.1 nm in diameter possessed the relaxivities of 18.49, 16.22, and 12.26 mM^{-1} s^{-1}, respectively, indicating significant increases as compared to that of Gd-DTPA (3.24 mM^{-1} s^{-1}) (Figure 2B). Remarkably, Gd$_2$O$_3$@albumin exhibit much stronger signals than Gd-DTPA, which might result from the formation of Gd$_2$O$_3$ with relatively suitable size. Subsequently, Gd$_2$O$_3$@albumin were further conjugated with Ce6, a typical PS through the carbodiimide coupling strategy, followed by the formation of Gd$_2$O$_3$@albumin conjugating PS (GA-NPs). The conjugation was further validated by their FT-IR spectra with characteristic peaks of Ce6 (Figure 2C). GA-NPs was found to have the drug loading level of 5.5% for Ce6. Moreover, given that photostability may affect the efficiency of PS, we further evaluated the photostability of GA-NPs under irradiation. The absorbance spectra show that free Ce6 exhibited a quick decrease of absorbance within 2 min owing to its rapid photobleaching (Figure 2D), while GA-NPs can effectively improve the photostability of Ce6, possibly owing to their effective protection of unsaturated bonds of Ce6 from the damage of ROS.[12] Subsequently, we evaluated the chemical stability of PS in GA-NPs. Figure S4 shows that GA-NPs exhibited a good chemical stability of Ce6 in PBS containing 10% fetal bovine serum (FBS) at pH 7.4 as compared to free Ce6, indicating that the albumin nanoreactor may maintain a stable structure in aqueous environment, and thus protect Ce6 from chemical degradation. The singlet oxygen quantum yield (Φ_Δ) of GA-NPs was evaluated using zinc phthalocyanine (ZnPc, Φ_Δ = 0.56 in dimethyl formamide) as a reference under 660 nm irradiation. Figure S5 shows that GA-NPs exhibited the singlet oxygen quantum yield of 0.1. To explore the ability of GA-NPs to generate singlet oxygen under irradiation, we irradiated GA-NPs in an aqueous solution using 1,3-diphenyliso-benzofuran (DPBF) as a probe, which can be specifically quenched by singlet oxygen.[12] Figure 2E shows that GA-NPs produced a detectable amount of singlet oxygen from Ce6 even at a dose of 1.0 μg mL^{-1} under 660 nm irradiation (0.8 W cm^{-2}), and also exhibited a concentration-dependent generation of singlet oxygen in aqueous solution, indicating that GA-NPs are highly capable of generating singlet oxygen even at a low concentration. Interestingly, GA-NPs exhibited the temperature elevation of ~6.0 °C in 300 s at the concentration of 2.0 μg mL^{-1} Ce6
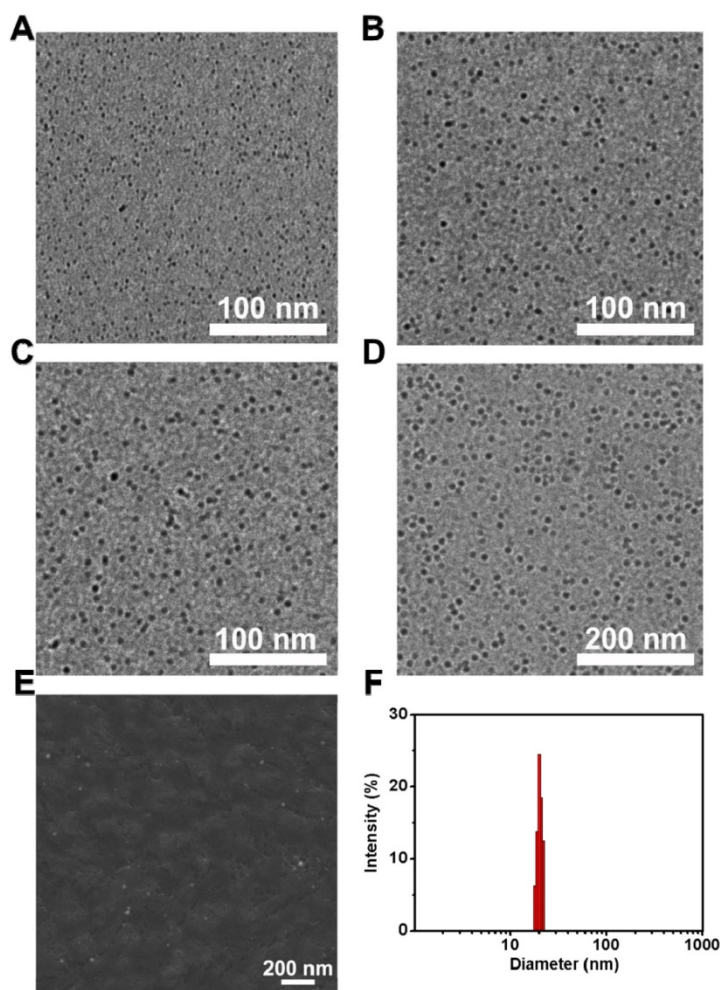

Figure 1. TEM images of Gd$_2$O$_3$@albumin synthesized from various reaction time including A) 1 h, B) 4 h, C) 8 h, and D) 12 h, respectively. E) SEM image of Gd$_2$O$_3$@albumin synthesized from 12 h reaction time. F) Hydrodynamic diameter of Gd$_2$O$_3$@albumin synthesized from 12 h reaction time.

under 660 nm irradiation at 0.8 W cm^{-2}, and also possess a concentration-dependent photothermal effect (Figure 2F). Distinctly, GA-NPs cause both abundant ROS and potent photothermal effect under 660 nm irradiation at 0.8 W cm^{-2}, which is highly advantageous to achieve PDT/PTT efficiency.

Cellular Uptake, Intracellular ROS, Photo-cytotoxicity, and Lysosomal Disruption

To demonstrate whether GA-NPs can be internalized by cancer cells, we evaluated their cellular uptakes by the 4T1 murine breast cancer cells. Figure 3A shows that GA-NPs exhibited the time-dependent cellular uptakes, and had a 1.7-fold increase of the cellular uptake of Ce6 after 24 h incubation as compared to free Ce6, indicating that

GA-NPs can effectively improve the cellular uptake of PS. Subsequently, we further observe the ability of GA-NPs to generate intracellular ROS using dihydroethidium (DHE) staining, which can emit red fluorescence in the presence of singlet oxygen.[38] It shows that the red fluorescence was observed from the cells treated with GA-NPs at the dose of 0.1 µg mL^{-1} Ce6 under irradiation, while there was no fluorescence from the cells in the absence of irradiation (Figure S6). Furthermore, higher concentrations of GA-NPs further resulted in stronger red fluorescence under irradiation, indicating that GA-NPs exhibit a concentration-dependent generation of intracellular ROS, which plays a key role for causing cell damage.
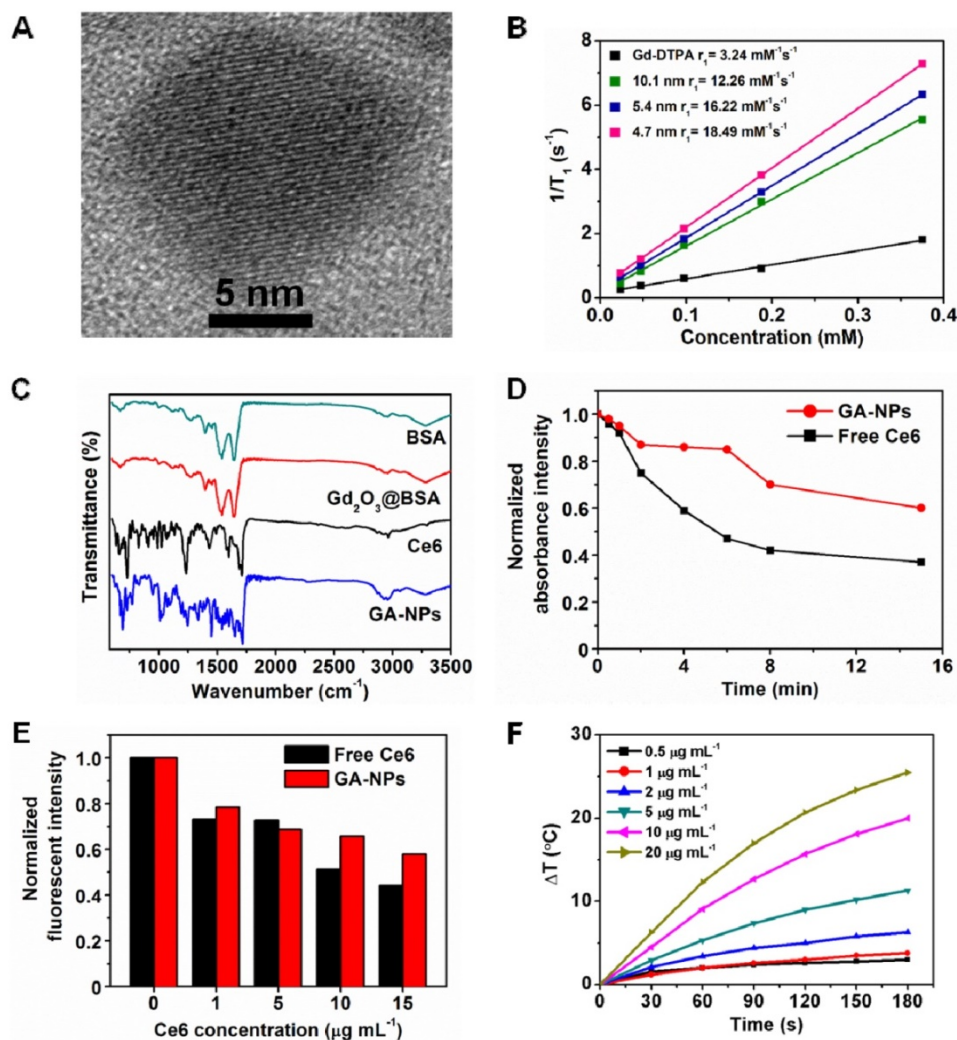

Figure 2. A) HR-TEM image of GA-NPs. B) Relaxivity values of GA-NPs with various size and Gd-DTPA. C) FT-IR spectra of GA-NPs. D) Photostability of 10.1 nm GA-NPs and free Ce6 in aqueous solution under irradiation (660 nm, 0.8 W cm^{-2}). E) Normalized fluorescent intensity of DPBF after trapping singlet oxygen from 10.1 nm GA-NPs and free Ce6 at various concentrations of Ce6 under 660 nm irradiation at 0.8 W cm^{-2}. F) Photothermal heating curves of 10.1 nm GA-NPs at various Ce6 concentrations under irradiation (660 nm, 0.8 W cm^{-2}).
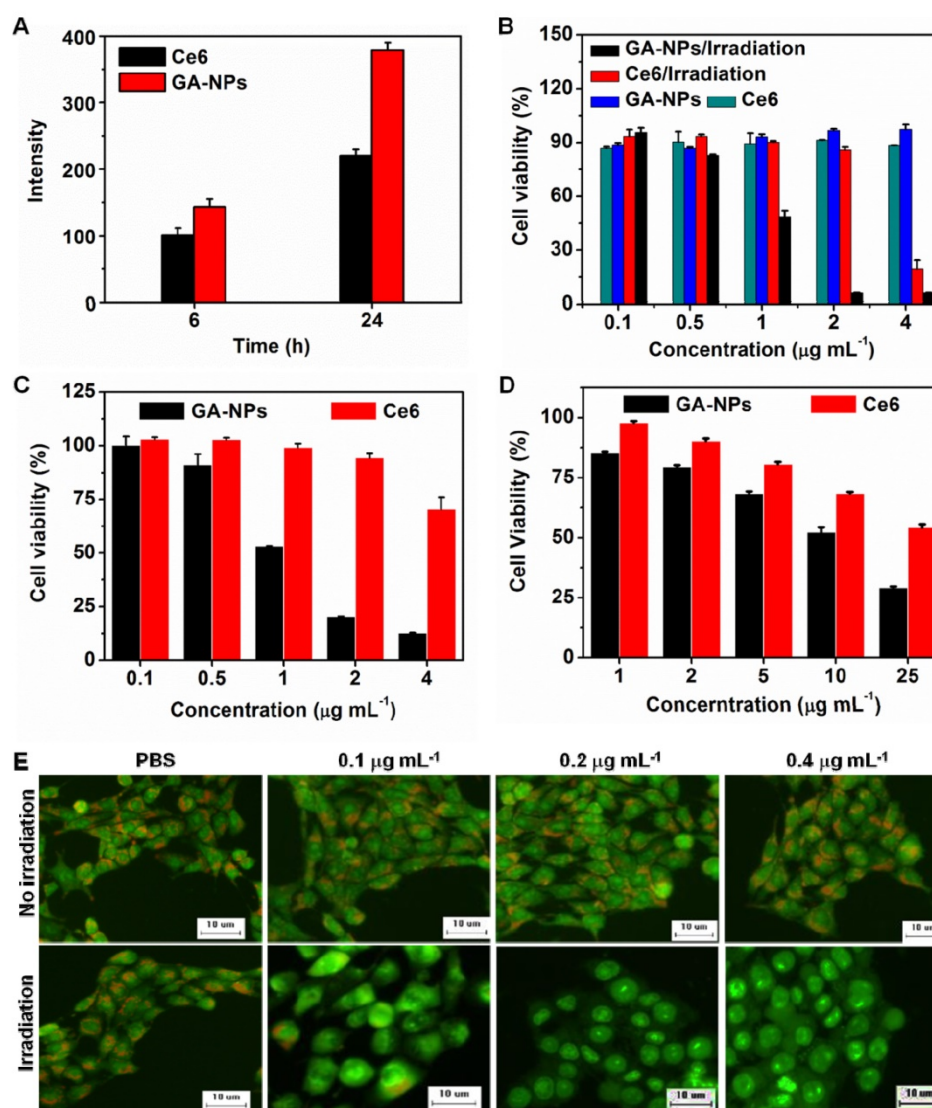
Figure 3. A) Amounts of internalized free Ce6 and 10.1 nm GA-NPs by 4T1 cells after 6 h and 24 h incubation, respectively. B) Relative viabilities of 4T1 cells incubated with free Ce6 and 10.1 nm GA-NPs for 24 h with or without 5 min irradiation (660 nm, 0.8 W cm⁻²), respectively. C) Relative viability of 4T1 cells incubated with 10.1 nm GA-NPs and free Ce6 for 24 h under 25 min irradiation (660 nm, 0.15 W cm⁻²), respectively. D) Relative viability of 4T1 cells incubated with 10.1 nm GA-NPs and free Ce6 in the presence of 1.0 mM Vitamin C (Vc) for 24 h under 5 min irradiation (660 nm, 0.8 W cm⁻²), respectively. E) Observation of lysosomal disruption of 4T1 cells treated with 10.1 nm GA-NPs at various concentrations of Ce6 using AO staining with or without 5 min irradiation (660 nm, 0.8 W cm⁻²).

To examine the photo-induced cytotoxicity of GA-NPs, we incubated 4T1 cells with GA-NPs for 24 h, followed by 660 nm irradiation or not (5 min, 0.8 W cm⁻²). GA-NPs acted as a non-toxic agent in the absence of irradiation owing to their negligible cytotoxicity (Figure 3B). However, GA-NPs generated severe photo-induced damage against 4T1 cells (~0.9 µg mL⁻¹ IC$_{50}$) under irradiation, which was much lower than that of free Ce6 (~3.0 µg mL⁻¹) (Figure 3B). To evaluate the photodynamic damage of the nanoparticles in the absence of photothermal effect, we evaluated the cytotoxicity of the nanoparticles under 660 nm irradiation at 0.15 W cm⁻² for 25 min. Figure 3C shows that GA-NPs had the cytotoxicity with IC50 of 1.3 µg mL⁻¹ Ce6, indicating a slightly reduced cytotoxicity as compared to that (0.9 µg mL⁻¹

Ce6) under 660 nm irradiation (5 min, 0.8 W cm⁻²). The photothermal damage of GA-NPs might slightly contribute to the cytotoxicity in the dose range of less than 4.0 µg mL⁻¹ Ce6. To further distinguish the contribution of photothermal damage to the cytotoxicity under 660 nm irradiation at 0.8 W cm⁻², we incubated both GA-NPs and reactive oxygen species (ROS)-scavenger Vitamin C (Vc) with 4T1 cells, followed by 660 nm irradiation at 0.8 W cm⁻² for 5 min and subsequent MTT assay. As shown in Figure 3D, GA-NPs exhibited the distinctly reduced cytotoxicity with IC50 of 13.2 µg mL⁻¹ Ce6 in the presence of Vc, suggesting that GA-NPs have remarkable photothermal cell damage at higher doses of Ce6. As a consequence, GA-NPs primarily possess photodynamic cytotoxicity at relatively low doses of

Ce6 under irradiation, while higher doses cause remarkable photothermal damage. It indicates that GA-NPs can effectively generate severe photo-cytotoxicity, probably owing to enhanced cellular uptake of Ce6 and effective singlet oxygen, and photothermal effect.

Moreover, we further explored the influence of GA-NPs on the lysosomes using acridine orange (AO) as an intracellular indicator.[39, 40] Figure 3E shows that the lysosomes in 4T1 cells treated with PBS revealed red fluorescence under irradiation, which was similar to that of PBS without irradiation. Remarkably, the lysosomes were intact in the absence of GA-NPs regardless of irradiation. However, the red fluorescence from AO was remarkably decreased in the presence of GA-NPs at the dose of 0.1 µg mL^{-1} Ce6 upon irradiation. Distinctly, GA-NPs can more effectively disrupt the lysosomal membranes even at a low dose of Ce6 as compared to free Ce6 (Figure S7), possibly owing to the damage from intracellular ROS from Ce6 upon irradiation. The lysosomal disruption can facilitate the translocation of GA-NPs and singlet oxygen from the lysosomes to cytoplasm, which can contribute to the enhanced photo-cytotoxicity through the enhanced accessibility of singlet oxygen to the target organelles such as nucleus and mitochondria.[40] Moreover, this disruption is able to cause the release of lysosomal enzymes into cytoplasm and prevent cancer cells from autophagy-based rescue, thereby facilitating cell apoptosis.[41, 42] More interestingly, the disruption of lysosomal membranes generally results from the photochemical internalization effect of singlet oxygen from amphiphilic PS such as indocyanine green and AlPcS$_{2a}$ on the lysosomal membranes, since this type of PS can easily co-localize with lysosomal membranes and thus easily lead to the direct oxidative damage of singlet oxygen on the membranes.[8, 40, 43] The effective lysosomal disruption from GA-NPs containing hydrophobic PS implies that GA-NPs can allow hydrophobic PS to provide sufficient intracellular singlet oxygen for damaging the lysosomes in addition to amphiphilic PS.[8] Consequently, GA-NPs as a nanocarrier can effectively generate intracellular ROS, photothermal effect, and subsequent intracellular translocation under irradiation, which might synergistically contribute to the enhanced photo-cytotoxicity.[43]

Biodistribution

We evaluated the biodistribution behavior of GA-NPs with various particle size on the mice bearing 4T1 tumors. 10.1 nm GA-NPs exhibited preferable tumor accumulations of Gd at 24 h post-injection as compared to those with 4.7 nm and 5.4 nm in diameter (Figure 4A), indicating that GA-NPs have size-dependent tumor accumulation. Moreover, the tumor accumulations of 10.1 nm GA-NPs were also evaluated on the 4T1 tumor-bearing mice at various time. It shows that 10.1 nm GA-NPs also had time-dependent accumulations of Gd at tumor (Figure 4B). Meanwhile, GA-NPs with 10.1 nm in diameter also resulted in a 10-fold increase of Ce6 amount at the tumor site at 24 h post-injection as compared to free Ce6 (Figure S8). Distinctly, GA-NPs have a good targeting capacity, possibly owing to their enhanced permeation and retention (EPR) effect. The enhanced tumor accumulations are highly advantageous to generate enhanced imaging contrast, and sufficient intracellular ROS under irradiation. In addition, the small diameter of GA-NPs might also contribute to deep penetration at tumor, thereby facilitating the uniform distribution of GA-NPs in the tumor.[36]

In Vivo MRI Studies

To evaluate the MRI capacity of GA-NPs with various size, we performed T_1-weight MR imaging at the magnetic field of 1.5 T on the mice bearing 4T1 tumor. All the GA-NPs had continuous increases of imaging intensities at tumors during 24 h post-injection as compared to Gd-DTPA, while they showed no significant change of imaging intensity at normal tissues such as muscles (Figure 4C-F and Figure S9). It indicates that GA-NPs possess strong MR imaging capability with enhanced contrast. In particular, GA-NPs with 10.1 nm in diameter exhibited highest imaging intensity during 24 h post-injection (Figure 4F). Possibly, the preferable tumor accumulation of largest GA-NPs primarily accounts for their enhanced imaging capacity,[36] even though they have relatively low relaxivity. Therefore, GA-NPs are able to act as an effective MRI agent for T_1-weight imaging with enhanced imaging contrast for precise tumor localization and PDT treatment guidance.[44-46] In addition, the Gd$_2$O$_3$ nanocrystals are integrated within the hollow cavity of GA-NPs conjugating Ce6, and thus imaging agent and PS are not easily be released from the nanoparticles, implying that MRI can also have a potential capacity to visualize the *in vivo* distribution of PS and therapeutic performance.[12]

In Vivo Hyperthermia and Anticancer Efficacy

We performed the *in vivo* hyperthermia using infrared thermography (Figure 5A and 5B). It shows that GA-NPs resulted in the temperature elevation of 13°C at tumor, indicating a potent hyperthermia owing to their remarkable photothermal effect and enhanced tumor accumulation. Therefore, GA-NPs are potentially able to achieve PTT treatment under

irradiation in addition to PDT treatment. To demonstrate the *in vivo* anticancer efficacy, GA-NPs were injected into the mice bearing 4T1 tumor at a single dose of 5 mg kg^{-1} Ce6, and then the tumors were irradiated at 24 h post-injection (5 min, 0.8 W cm^{-2}). Next, the tumor volumes were measured during subsequent 12 days (Figure 5C and 5D). PBS as a control resulted in 3.5 ~ 4.0-fold increases of tumor volumes compared to their original volumes in the absence or presence of irradiation, implying that the irradiation itself does not affect the tumor growth.

GA-NPs and free Ce6 also exhibited similar tumor growth to those of PBS group without irradiation, indicating that GA-NPs act as inactive agents in the absence of irradiation. Interestingly, GA-NPs only exhibited 1.8-fold increase of tumor volumes as compared to their original volumes in the presence of ROS-scavenger Vc in the tumor under irradiation, indicating that only the hyperthermia cause remarkable anticancer efficacy in the absence of singlet oxygen, and the photothermal damage plays an important role in the tumor ablation.
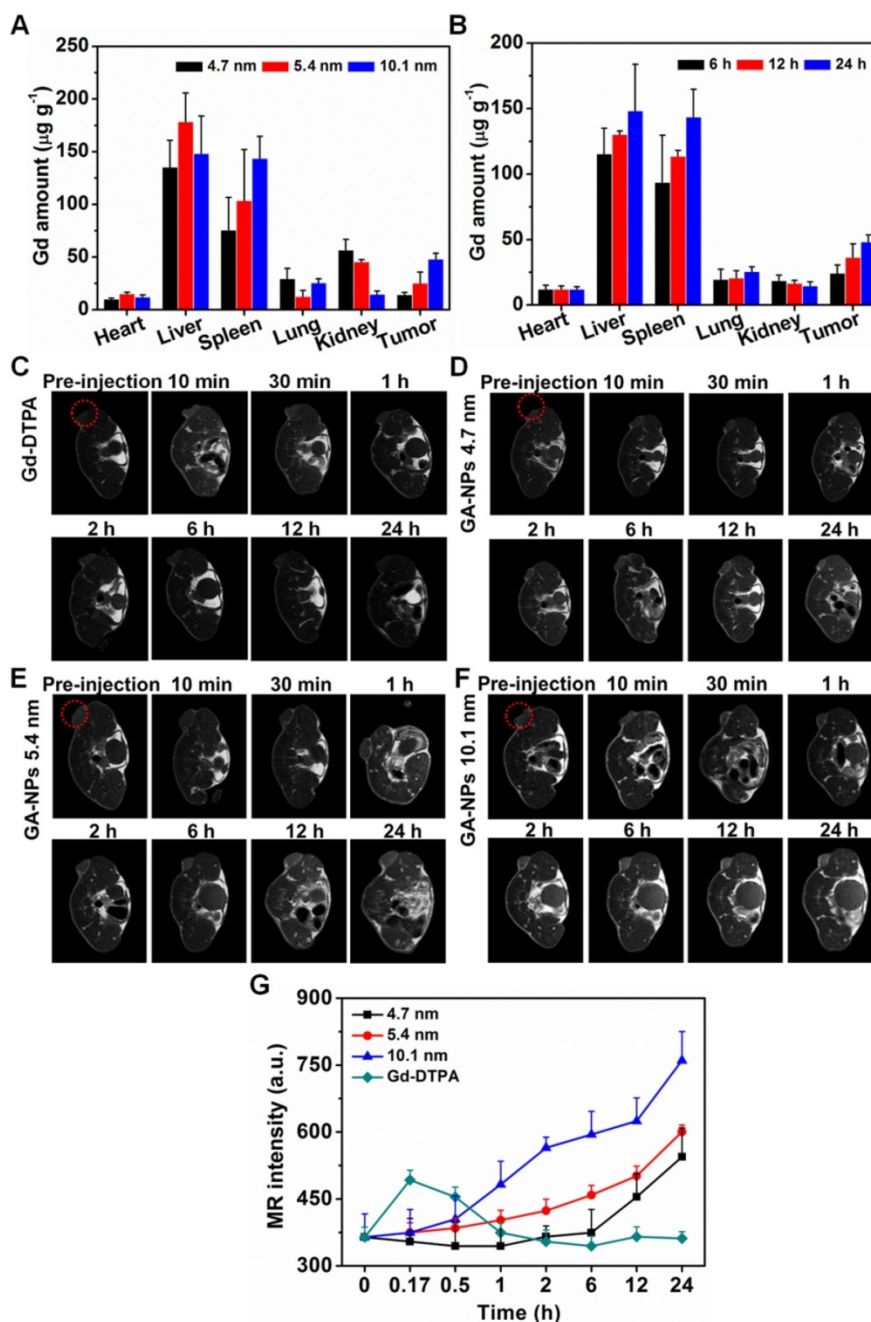

Figure 4. A) Bioistribution of Gd at various tissues of the 4T1 tumor-bearing mice treated with GA-NPs with various size at the dose of 0.5 mmol Gd kg^{-1} at 24 h post-injection. B) Biodistribution of Gd at various tissues of the 4T1 tumor-bearing mice treated with GA-NPs with 10.1 nm in diameter at the dose of 0.5 mmol Gd kg^{-1} at 6, 12, 24 h post-injection, respectively. *In vivo* MRI images of the mice bearing 4T1 tumor treated with C) Gd-DTPA, D) 4.7 nm GA-NPs, E) 5.4 nm GA-NPs, F) 10.1 nm GA-NPs, and G) their signal intensities in the tumors at pre-injection, 10 min, 0.5 h, 1 h, 2 h, 6 h, 12 h, and 24 h post-injection, respectively.
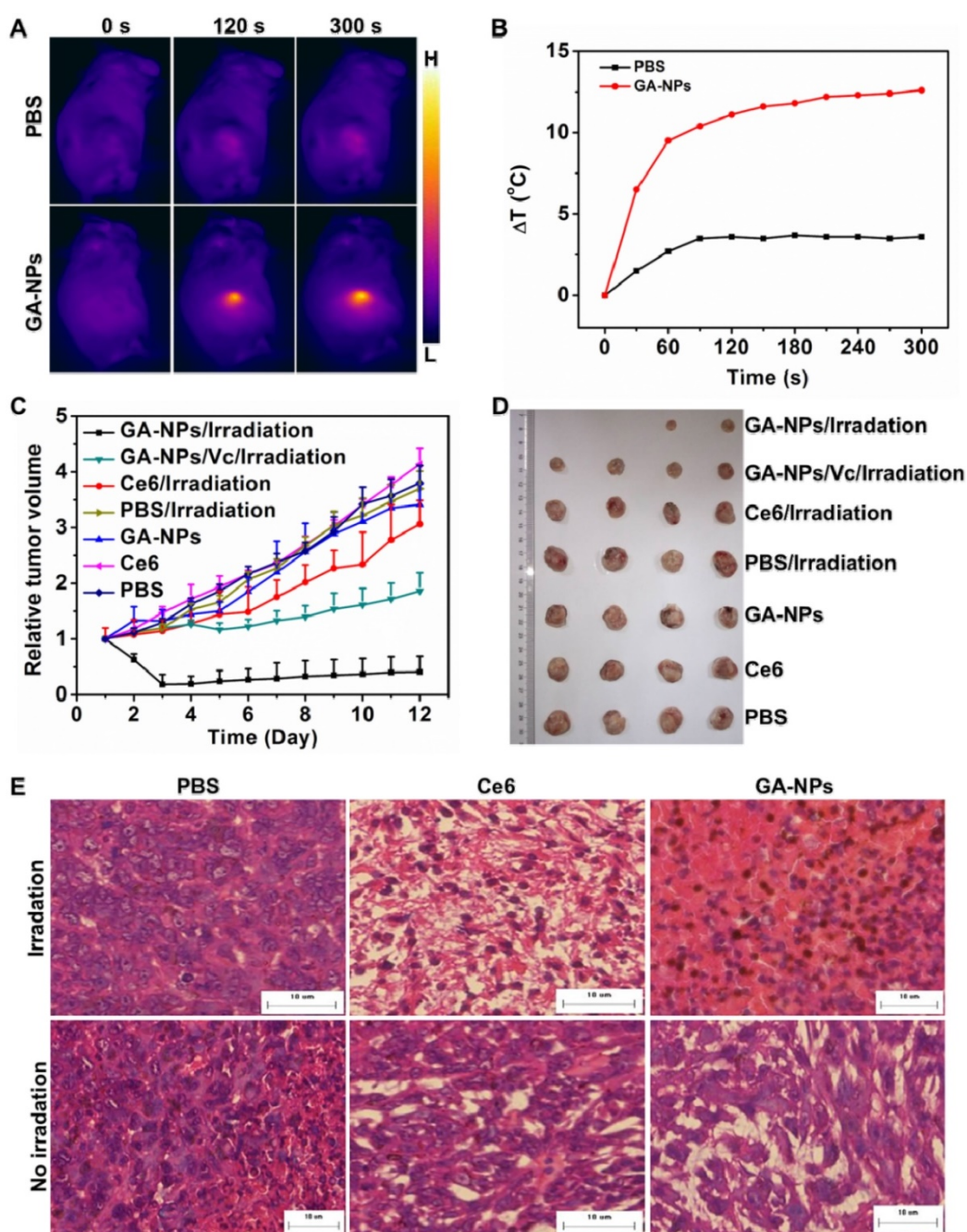
Figure 5. A) Infrared thermography, and B) tumor temperature of tumor-bearing mice treated with 10.1 nm GA-NPs at the dose of 5 mg kg^{-1} at 24 h post-injection under 660 nm irradiation at 0.8 W cm^{-2}. C) Tumor growth inhibition profiles of the mice bearing 4T1 tumor treated with 10.1 nm GA-NPs and free Ce6 at the dose of 5 mg kg^{-1}, followed by 660 nm irradiation at 0.8 W cm^{-2} for 5 min, and D) photos of the tumors extracted from the mice bearing 4T1 tumor at the end of the experiment. E) Images of H&E-stained tumor sections harvested from the mice treated with PBS, free Ce6, and 10.1 nm GA-NPs at 6 h post-irradiation (5 min, 660 nm, 0.8 W cm^{-2}), respectively (bar: 10 μm).

Importantly, GA-NPs exhibited much more remarkable photo-induced damage against the tumors under irradiation, which resulted in immediate tumor regress after 2 days post-injection, and even ablation of some tumors during 12 days post-injection (Figure 5C), which is in agreement with the enhanced *in vitro* photo-cytotoxicity. It suggests that both photodynamic and photothermal damages of GA-NPs synergistically contributed to their potent anticancer efficacy. However, free Ce6 as a control also exhibited obvious tumor growth after 6 days post-injection, and finally resulted in a 3-fold increase of tumor volumes (Figure 5D). It indicates that free Ce6 has a poor anticancer efficacy, possibly resulting from its low photo-cytotoxicity and insufficient tumor accumulation. As a result, GA-NPs exhibit more significant photo-damage against the tumors as compared to free Ce6, probably owing to their enhanced tumor accumulation, and preferable photo-induced cytotoxicity.[12] In addition, the deep

penetration of GA-NPs in the tumor can also facilitate the homogeneity of ROS at tumor under irradiation, thereby contributing to the enhanced anticancer efficacy.

Ex Vivo Histological Staining

To further elucidate the *in vivo* PDT damage of GA-NPs on the tumors under irradiation, GA-NPs and free Ce6 were injected into the mice bearing 4T1 tumor at a single dose of 5 mg kg^{-1} Ce6, and then the tumors were irradiated for 5 min at 24 h post-injection, followed by Hematoxylin and Eosin (H&E) staining of tumor sections at 6 h post-irradiation. Figure 5E shows that GA-NPs caused severe cell destruction and severe hemorrhagic inflammation under irradiation, while free Ce6 only exhibited hemorrhagic inflammation.[12, 43] PBS as a control did not cause obvious tumor damage in the absence or presence of irradiation. In addition, GA-NPs exhibited no obvious injury on the normal tissues including heart, liver, spleen, lung and kidney (Figure S10), implying that PDT treatment has no influence on the normal tissues.

Conclusion

In summary, we demonstrate a facile synthesis of theranostic GA-NPs using hollow albumin as a nanoreactor for MRI-guided photo-induced therapy. In the nanoreactor, the reaction time can effectively regulate the growth of Gd_2O_3 nanocrystals within the hollow cavity of the nanoreactor, which can achieve the suitable hydrodynamic diameter of 25.0 nm, and preferable longitudinal relaxivity through their size control. The nanoreactor is easily conjugated with PS (e.g. Ce6) for photo-induced therapy, followed by the formation of GA-NPs. GA-NPs exhibited the enhanced cellular uptake, sufficient intracellular ROS under irradiation, potent photothermal effect, as well as effective subcellular translocation *via* the disruption of lysosomes, which synergistically contributed to the enhanced photo-induced cytotoxicity. As a consequence, GA-NPs with enhanced tumor accumulation possess a desirable *in vivo* MRI capacity with enhanced imaging contrast for precise tumor localization, and simultaneously exhibit potent PDT/PTT efficacy under irradiation. Our design of albumin nanoparticles represents a promising versatile approach to fabricate theranostic nanocarrier for cancer imaging and simultaneous therapy.

Experimental Section

Detailed experimental materials and methods can be found in the Supporting Information.

Supplementary Material

Experiment sections and supplementary figures.
http://www.thno.org/v07p0764s1.pdf

Competing Interests

The authors have declared that no competing interest exists.

References

1. Chatterjee DK, Fong LS, Zhang Y. Nanoparticles in photodynamic therapy: An emerging paradigm. Adv Drug Deliv Rev. 2008; 60: 1627-37.
2. Yano S, Hirohara S, Obata M, Hagiya Y, Ogura S-i, Ikeda A, et al. Current states and future views in photodynamic therapy. J Photoch Photobio C. 2011; 12: 46-67.
3. Yang K, Feng L, Shi X, Liu Z. Nano-graphene in biomedicine: theranostic applications. Chem Soc Rev. 2013; 42: 530-47.
4. Zha Z, Yue X, Ren Q, Dai Z. Uniform polypyrrole nanoparticles with high photothermal conversion efficiency for photothermal ablation of cancer cells. Adv Mater. 2013; 25: 777-82.
5. Lal S, Clare SE, Halas NJ. Nanoshell-enabled photothermal cancer therapy: impending clinical impact. Acc Chem Res. 2008; 41: 1842-51.
6. Luo S, Zhang E, Su Y, Cheng T, Shi C. A review of NIR dyes in cancer targeting and imaging. Biomaterials. 2011; 32: 7127-38.
7. Shafirstein G, Battoo A, Harris K, Baumann H, Gollnick SO, Lindenmann J, et al. Photodynamic therapy of non–small cell lung cancer. Narrative review and future directions. Ann Am Thorac Soc. 2015; 13: 265-75.
8. Castano AP, Demidova TN, Hamblin MR. Mechanisms in photodynamic therapy: part one—photosensitizers, photochemistry and cellular localization. Photodiagnosis Photodyn Ther. 2004; 1: 279-93.
9. Castano AP, Demidova TN, Hamblin MR. Mechanisms in photodynamic therapy: part two—cellular signaling, cell metabolism and modes of cell death. Photodiagnosis Photodyn Ther. 2005; 2: 1-23.
10. Castano AP, Demidova TN, Hamblin MR. Mechanisms in photodynamic therapy: Part three—photosensitizer pharmacokinetics, biodistribution, tumor localization and modes of tumor destruction. Photodiagnosis Photodyn Ther. 2005; 2: 91-106.
11. Chen H, Tian J, He W, Guo Z. H_2O_2-activatable and O_2-evolving nanoparticles for highly efficient and selective photodynamic therapy against hypoxic tumor cells. J Am Chem Soc. 2015; 137: 1539-47.
12. Guo M, Mao H, Li Y, Zhu A, He H, Yang H, et al. Dual imaging-guided photothermal/photodynamic therapy using micelles. Biomaterials. 2014; 35: 4656-66.
13. Wang J, Zhu G, You M, Song E, Shukoor MI, Zhang K, et al. Assembly of aptamer switch probes and photosensitizer on gold nanorods for targeted photothermal and photodynamic cancer therapy. ACS Nano. 2012; 6: 5070-7.
14. Wang S, Huang P, Nie L, Xing R, Liu D, Wang Z, et al. Single continuous wave laser induced photodynamic/plasmonic photothermal therapy using photosensitizer-functionalized gold nanostars. Adv Mater. 2013; 25: 3055-61.
15. Chen R, Wang X, Yao X, Zheng X, Wang J, Jiang X. Near-IR-triggered photothermal/photodynamic dual-modality therapy system via chitosan hybrid nanospheres. Biomaterials. 2013; 34: 8314-22.

16. Oh J, Yoon H, Park HJ. Nanoparticle platforms for combined photothermal and photodynamic therapy. Biomed Eng Lett. 2013; 3: 67-73.
17. Huang H, Yu B, Zhang P, Huang J, Chen Y, Gasser G, et al. Highly charged ruthenium(II) polypyridyl complexes as lysosome-localized photosensitizers for two-photon photodynamic therapy. Angew Chem Int Ed Engl. 2015; 54: 14049-52.
18. Hu Y, Yang Y, Wang H, Du H. Synergistic integration of layer-by-layer assembly of photosensitizer and gold nanorings for enhanced photodynamic therapy in the near infrared. ACS Nano. 2015; 9: 8744-54.
19. Cheng Y, Cheng H, Jiang C, Qiu X, Wang K, Huan W, et al. Perfluorocarbon nanoparticles enhance reactive oxygen levels and tumour growth inhibition in photodynamic therapy. Nat Commun. 2015; 6: 8785.
20. Chouikrat R, Seve A, Vanderesse R, Benachour H, Barberi-Heyob M, Richeter S, et al. Non polymeric nanoparticles for photodynamic therapy applications: recent developments. Curr Med Chem. 2012; 19: 781-92.
21. Park Y, Kim HM, Kim JH, Moon KC, Yoo B, Lee KT, et al. Theranostic probe based on lanthanide-doped nanoparticles for simultaneous in vivo dual-modal imaging and photodynamic therapy. Adv Mater. 2012; 24: 5755-61.
22. Josefsen LB, Boyle RW. Unique diagnostic and therapeutic roles of porphyrins and phthalocyanines in photodynamic therapy, imaging and theranostics. Theranostics. 2012; 2: 916-66.
23. Liang XL, Li XD, Jing LJ, Yue XL, Dai ZF. Theranostic porphyrin dyad nanoparticles for magnetic resonance imaging guided photodynamic therapy. Biomaterials. 2014; 35: 6379-88.
24. Xie JP, Zheng YG, Ying JY. Protein-directed synthesis of highly fluorescent gold nanoclusters. J Am Chem Soc. 2009; 131: 888-89.
25. Chen Q, Liang C, Wang C, Liu Z. An imagable and photothermal "Abraxane-Like" nanodrug for combination cancer therapy to treat subcutaneous and metastatic breast tumors. Adv Mater. 2015; 27: 903-10.
26. Yang JJ, Yang JH, Wei LX, Zurkiya O, Yang W, Li SY, et al. Rational design of protein-based MRI contrast agents. J Am Chem Soc. 2008; 130: 9260-7.
27. Huang P, Rong PF, Jin A, Yan XF, Zhang MG, Lin J, et al. Dye-loaded ferritin nanocages for multimodal imaging and photothermal therapy. Adv Mater. 2014; 26: 6401-8.
28. Sun CJ, Yang H, Yuan Y, Tian X, Wang LM, Guo Y, et al. Controlling assembly of paired gold clusters within apoferritin nanoreactor for in vivo kidney targeting and biomedical imaging. J Am Chem Soc. 2011; 133: 8617-24.
29. Jeong H, Huh M, Lee SJ, Koo H, Kwon IC, Jeong SY, et al. Photosensitizer-conjugated human serum albumin nanoparticles for effective photodynamic therapy. Theranostics. 2011; 1: 230-9.
30. Tanford C, Buzzell JG, Rands DG, Swanson SA. The reversible expansion of bovine serum albumin in acid solutions. J Am Chem Soc. 1955; 77: 6421-8.
31. Fan KL, Cao CQ, Pan YX, Lu D, Yang DL, Feng J, et al. Magnetoferritin nanoparticles for targeting and visualizing tumour tissues. Nat Nanotechnol. 2012; 7: 833-76.
32. Liang MM, Fan KL, Zhou M, Duan DM, Zheng JY, Yang DL, et al. H-ferritin-nanocaged doxorubicin nanoparticles specifically target and kill tumors with a single-dose injection. Proc Natl Acad Sci USA. 2014; 111: 14900-5.
33. Zhang BB, Jin HT, Li Y, Chen BD, Liu SY, Shi DL. Bioinspired synthesis of gadolinium-based hybrid nanoparticles as MRI blood pool contrast agents with high relaxivity. J Mater Chem. 2012; 22: 14494-501.
34. Sun C, Yuan Y, Xu Z, Ji T, Tian Y, Wu S, et al. Fine-tuned H-ferritin nanocage with multiple gold clusters as near-infrared kidney specific targeting nanoprobe. Bioconjug Chem. 2015; 26: 193-6.
35. Bro P, Singer SJ, Sturtevant JM. On the aggregation of bovine serum albumin in acid solutions. J Am Chem Soc. 1958; 80: 389-93.
36. Wang Y, Yang T, Ke HT, Zhu AJ, Wang YY, Wang JX, et al. Smart albumin-biomineralized nanocomposites for multimodal imaging and photothermal tumor ablation. Adv Mater. 2015; 27: 3874-82.
37. Tsung CK, Kuhn JN, Huang WY, Aliaga C, Hung LI, Somorjai GA, et al. Sub-10 nm platinum nanocrystals with size and shape control: catalytic study for ethylene and pyrrole hydrogenation. J Am Chem Soc. 2009; 131: 5816-22.
38. Li Y, Deng Y, Tian X, Ke H, Guo M, Zhu A, et al. Multipronged design of light-triggered nanoparticles to overcome cisplatin resistance for efficient ablation of resistant tumor. ACS Nano. 2015; 9: 9626-37.
39. Zhu A, Miao K, Deng Y, Ke H, He H, Yang T, et al. Dually pH/reduction-responsive vesicles for ultrahigh-contrast fluorescence imaging and thermo-chemotherapy-synergized tumor ablation. ACS Nano. 2015; 9: 7874-85.
40. Chen HB, Xiao L, Anraku Y, Mi P, Liu XY, Cabral H, et al. Polyion complex vesicles for photoinduced intracellular delivery of amphiphilic photosensitizer. J Am Chem Soc. 2014; 136: 157-63.
41. Repnik U, Turk B. Lysosomal-mitochondrial cross-talk during cell death. Mitochondrion. 2010; 10: 662-9.
42. Boya P, Kroemer G. Lysosomal membrane permeabilization in cell death. Oncogene. 2008; 27: 6434-51.
43. Wan ZH, Mao HJ, Guo M, Li YL, Zhu AJ, Yang H, et al. Highly efficient hierarchical micelles integrating photothermal therapy and singlet oxygen-synergized chemotherapy for cancer eradication. Theranostics. 2014; 4: 399-411.
44. Park JY, Baek MJ, Choi ES, Woo S, Kim JH, Kim TJ, et al. Paramagnetic ultrasmall gadolinium oxide nanoparticles as advanced T_1 MRI contrast agent: account for large longitudinal relaxivity, optimal particle diameter, and in vivo T_1 MR images. ACS Nano. 2009; 3: 3663-9.
45. Li JX. Nanotechnology-based platform for early diagnosis of cancer. Sci Bull. 2015; 60: 488-90.
46. Sreejith S, Huong TTM, Borah P, Zhao Y. Organic-inorganic nanohybrids for fluorescence, photoacoustic and Raman bioimaging. Sci Bull. 2015; 60: 665-78.